

## Article

# Study on the Synthesis of LTA-Type Molecular Sieves from Coal Gangue and Aluminum Ash and Its Adsorption Properties towards $\text{Cu}^{2+}$

Qingping Wang <sup>1,2,3,\*</sup> , Wei Xu <sup>1</sup> , Jingyi Cai <sup>1,2</sup>, Qingbo Yu <sup>1</sup> and Jing Min <sup>1</sup>

<sup>1</sup> School of Materials Science and Engineering, Anhui University of Science and Technology, Huainan 232001, China

<sup>2</sup> Anhui Industrial Generic Technology Research Center for New Materials from Coal-Based Solid Wastes, Anhui University of Science and Technology, Huainan 232001, China

<sup>3</sup> State Key Laboratory of Mining Response and Disaster Prevention and Control in Deep Coal Mines, Anhui University of Science and Technology, Huainan 232001, China

\* Correspondence: wqp.507@163.com

**Abstract:** Coal gangue and aluminum ash emerge as quintessential constituents within the ambit of coal-derived solid waste and industrial residue, respectively. Leveraging coal gangue as a primary substrate and aluminum ash as an adjunct aluminum source, molecular sieves can be synthesized through hydrothermal means. By modulating the dosage of aluminum ash, molecular sieves with varying crystalline structures can be obtained. The synthesized LTA-type molecular sieves manifest in two distinct morphologies: regular tetrahedral and stratified spherical stacking, evincing commendable  $\text{Cu}^{2+}$  adsorption efficacy. The  $\text{Cu}^{2+}$  adsorption phenomenon predominantly transpires via chemisorption, albeit with ancillary manifestations of physical adsorption. The valorization of coal gangue and aluminum ash towards the synthesis of molecular sieves not only underscores the elevation of industrial solid waste towards high-value utility, but also underscores the praxis of waste remediation through upcycling.

**Keywords:** coal gangue; aluminum ash; LTA-type molecular sieves; regulating morphology; adsorption properties towards  $\text{Cu}^{2+}$



**Citation:** Wang, Q.; Xu, W.; Cai, J.; Yu, Q.; Min, J. Study on the Synthesis of LTA-Type Molecular Sieves from Coal Gangue and Aluminum Ash and Its Adsorption Properties towards  $\text{Cu}^{2+}$ . *Crystals* **2024**, *14*, 379. <https://doi.org/10.3390/cryst14040379>

Academic Editor: Volodymyr Bon

Received: 20 March 2024

Revised: 16 April 2024

Accepted: 16 April 2024

Published: 18 April 2024



**Copyright:** © 2024 by the authors. Licensee MDPI, Basel, Switzerland. This article is an open access article distributed under the terms and conditions of the Creative Commons Attribution (CC BY) license (<https://creativecommons.org/licenses/by/4.0/>).

## 1. Introduction

In light of resource endowment, energy infrastructure, and the developmental trajectory, China's future landscape in bulk solid waste management continues to confront a stark reality characterized by heightened generation intensity, suboptimal utilization practices, and diminished value-added output from comprehensive utilization endeavors. As per statistical data, the accumulated volume of bulk solid waste presently stockpiled in China approximates 600 billion metric tons, with an annual accrual of nearly 30 billion metric tons [1]. It is imperative to sustain efforts aimed at elevating the comprehensive utilization efficacy of coal gangue and pulverized coal ash, while concurrently intensifying the dissemination of high-volume blending practices and the adoption of high-value product applications. Furthermore, concerted endeavors are warranted to enhance industrial synergies, thereby progressively augmenting the overall utilization rate of smelting slag.

The industrial advancement in China has spurred the robust development of sectors such as coal mining, consequently engendering the generation of substantial quantities of coal-derived solid waste and industrial residues. Notable among these waste streams are coal gangue and aluminum ash. Coal gangue, a byproduct of coal extraction and beneficiation processes, constitutes approximately 10% to 15% of the aggregate coal production [2]. As per the China Ecological Environment Status Report, the raw coal output in China reached 4.56 billion metric tons in 2022, marking a 10.5% surge from 2021 [3]. Concurrently,

coal consumption escalated by 4.3% compared to 2021, with coal constituting 56.2% of the total energy consumption, reflecting a 0.3% increment from the previous year [3]. The concomitant rise in coal production and consumption portends a commensurate increase in coal gangue output annually. The accumulation of untreated coal gangue on the terrestrial surface not only engrosses land resources but also poses the hazard of leaching heavy metal ions [4], thereby contaminating soil and aquatic ecosystems [5–7].

As delineated in Figure 1, spanning the period from 2012 to 2023, notwithstanding fluctuations in coal gangue production, an overarching upward trajectory is discernible, while the utilization rate of coal gangue has persistently hovered around the 70% mark. Recent years have witnessed an uptick in the utilization rate of coal gangue, indicative of a heightened emphasis on its exploitation. Presently, the comprehensive utilization of coal gangue primarily pivots on the selection criterion predicated on carbon content and calorific value. Coal gangue characterized by high carbon content ( $\geq 20\%$ ) typically finds utility in power generation and thermal applications [8], whereas coal gangue with a lower carbon content ( $\leq 4\%$  or 4–6%) serves as feedstock for cement production, concrete aggregate [9], and various other construction materials, as well as backfill material in subsiding coal mining regions [10]. The concurrent mitigation of environmental degradation while augmenting the valorization of coal gangue through large-scale utilization remains a pivotal research frontier.

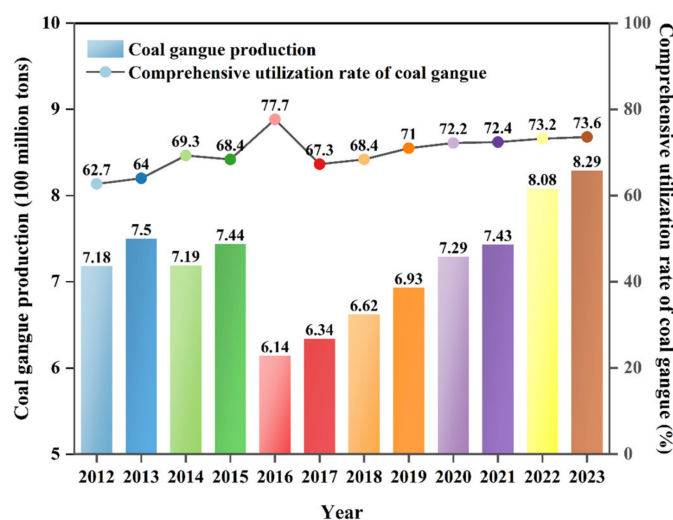


**Figure 1.** Coal gangue production and comprehensive utilization rate from 2012 to 2023.

Aluminum ash, a solid waste residue emanating from aluminum smelting and processing operations [11], harbors constituents such as aluminum oxide, aluminum nitride, and assorted oxides [12]. Mishandling of these components could precipitate grave environmental contamination [13]. It is documented that the production of one metric ton of aluminum metal yields an average of 15–25 kg of aluminum ash [14]. By the close of 2023, China’s primary aluminum output stood at 41.594 million metric tons, reflecting a 3.7% year-on-year escalation [15]. Based on Figure 2, it is evident that China has witnessed a substantial surge in electrolytic aluminum production from 2013 to 2023, with a persistent upward trajectory. In accordance with 2020 data, China’s annual aluminum ash production approximates 3 million metric tons. Hence, the imperative for a systematic exploration of the judicious utilization of aluminum ash is unmistakable.

Aluminum ash manifests a dual facet as hazardous solid waste and valuable resource reservoirs [11]. Nonetheless, at present, approximately 95% of aluminum ash undergoes direct landfill disposal [16], precipitating not only severe environmental degradation but also resource dissipation [17]. The current primary avenues for aluminum ash utilization primarily revolve around aluminum metal reclamation, characterized by a limited repertoire of methodologies, whereas secondary utilization schemes for aluminum ash

offer a more diversified landscape [18]. However, beyond aluminum metal recovery, alternative approaches for the resourceful utilization of aluminum ash remain incipient and intricately complex, with the majority entrenched in nascent laboratory-based research and development stages, thereby precluding their pragmatic application for industrial-scale deployment. Consequently, a comprehensive exploration of avenues for the resourceful utilization of aluminum ash warrants further scholarly inquiry.

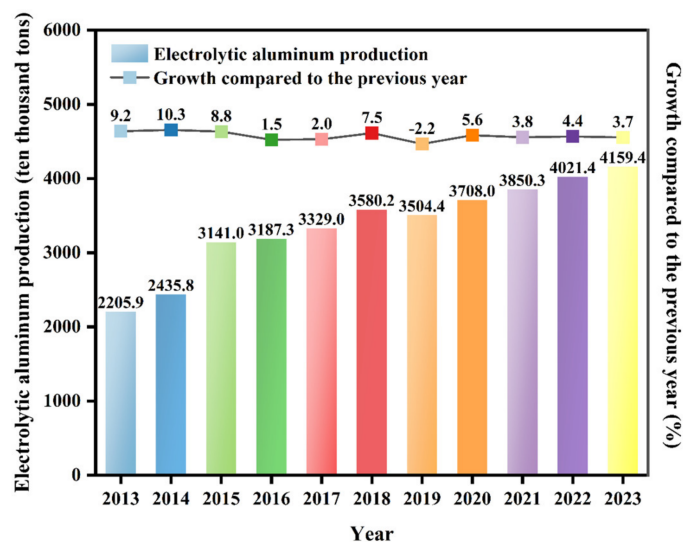


**Figure 2.** The production output and annual growth rate of electrolytic aluminum in China from 2013 to 2023.

Coal gangue, in addition to its residual carbon content, harbors a substantial abundance of silicon and aluminum constituents [19], whereas aluminum content in aluminum ash typically ranges from 35% to 60%. Consequently, both coal gangue and aluminum ash represent viable silicon–aluminum reservoirs for the synthesis of high-value-added zeolite molecular sieves [20]. Zeolite molecular sieves are framework silicate minerals characterized by a myriad of structural channels [21], comprising tetrahedral aluminum or silicon ions ( $\text{Al-O}_4$  or  $\text{Si-O}_4$ ). Numerous researchers have undertaken studies on synthesizing molecular sieves from coal-based solid wastes or other wastes [22–24], employing methods that have reached a relatively mature stage, including traditional hydrothermal synthesis [25], alkali fusion hydrothermal synthesis [26], and microwave-assisted synthesis [27]. The fundamental synthesis principles generally involve activating coal gangue to leach the requisite silicon–aluminum components, regulating parameters such as the silicon–aluminum ratio and sodium–silicon ratio, and obtaining precursors for aging. During aging at specific temperatures, there is a rearrangement of silicon–oxygen tetrahedra and aluminum–oxygen tetrahedra, leading to the formation of nuclei and gradually developing the framework structure of the molecular sieve. Following a certain aging period, the process progresses to the crystallization stage, where crystal growth occurs under appropriate temperature and pressure conditions, ultimately yielding the molecular sieve. In this regard, the alkali fusion hydrothermal synthesis method demonstrates enhanced efficacy in activating the silicon–aluminum constituents within coal gangue relative to conventional hydrothermal synthesis [28]. Furthermore, it presents lower energy consumption and streamlined operational procedures in contrast to microwave-assisted synthesis.

Notably, molecular sieves featuring low silicon–aluminum ratios demonstrate aptitude as effective adsorbents for heavy metals. In this study, aluminum ash is introduced as an exogenous aluminum source into processed coal gangue matrices, thus mitigating the silicon–aluminum ratio of the raw materials and facilitating the synthesis of LTA-type molecular sieves. By judiciously modulating the proportion of aluminum ash to coal gangue, a spectrum of LTA-type molecular sieves with diverse morphologies can

be tailored, thereby presenting a novel avenue for the valorization of coal gangue and aluminum ash toward high-value utilization endeavors.

## 2. Experiment

### 2.1. Experimental Reagents

The coal gangue powder employed in the experimental protocols originated from Huainan City, Anhui Province, China, while the aluminum ash was sourced from a designated enterprise situated in Wuhu City, Anhui Province, China. Analytical-grade sodium hydroxide (NaOH) was acquired from Sinopharm Chemical Reagent Co., Ltd. (Shanghai, China).

### 2.2. Preparation of Molecular Sieves

The coal gangue powder was subjected to calcination at 900 °C for 2 h within a muffle furnace. Post-calcination, the resultant product was homogeneously blended with sodium hydroxide (NaOH) powder at a mass ratio of 1:2. The amalgam was then introduced into a muffle furnace and co-fused at 500 °C for 2 h. Subsequently, 10.18 g of the co-fused powder was quantified and transferred into a 100 mL beaker, followed by the addition of 60 mL of deionized water. The amalgamation was magnetically stirred while incorporating varying quantities of untreated aluminum ash at distinct proportions until achieving uniformity.

The amalgamated raw materials were hermetically sealed with cling film and allowed to undergo static aging at 30 °C within a constant-temperature drying chamber for 4 h. Following thorough aging, the matured materials were transposed into a 100 mL reaction vessel and subjected to high-temperature crystallization at 110 °C within a constant-temperature drying chamber for 5 h. Upon completion, the samples were extracted from the reaction vessel and subjected to sequential washes until reaching a neutral state, followed by a 6 h desiccation period within a hot-air oven. Subsequently, the desiccated samples were pulverized to yield molecular sieve powder.

### 2.3. Adsorption Experiment of $\text{Cu}^{2+}$

Various concentrations of  $\text{Cu}^{2+}$  standard solutions were prepared utilizing copper nitrate. Following the addition of a copper ion chromogenic reagent, the absorbance at 452 nm was measured using a UV-visible spectrophotometer. The  $\text{Cu}^{2+}$  standard curve is depicted in Figure 3.

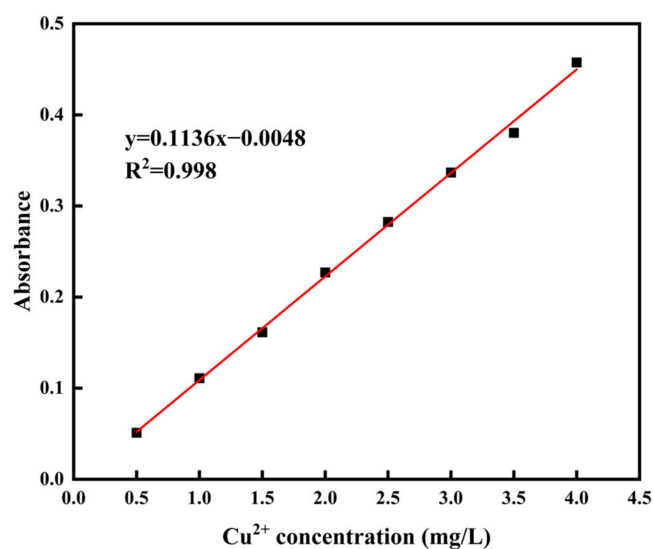


Figure 3.  $\text{Cu}^{2+}$  standard curve.

The prepared molecular sieve was utilized for adsorption experiments involving a  $\text{Cu}^{2+}$  solution with a concentration of 150 mg/L. Following the adsorption of the 150 mg/L

Cu<sup>2+</sup> solution by 0.1 g of molecular sieve, the resulting Cu<sup>2+</sup> concentration was quantified. The adsorption capacity ( $Q_t$ ) was subsequently determined using Equation (1).

$$Q_t = \frac{(c_0 - c_t) \times V}{m} \quad (1)$$

where  $Q_t$  denotes the adsorbed quantity of Cu<sup>2+</sup> (mg/g) at a given time  $t$  (min),  $C_0$  signifies the initial concentration of Cu<sup>2+</sup> in the solution prior to adsorption (mg/L),  $C_t$  represents the concentration of Cu<sup>2+</sup> in the solution at the adsorption time  $t$  (min) (mg/L),  $m$  signifies the mass of the molecular sieve (g), and  $V$  indicates the volume of the Cu<sup>2+</sup> solution (L).

The adsorption dataset underwent nonlinear fitting employing the pseudo-first-order kinetic model and the pseudo-second-order kinetic model. The pseudo-first-order kinetic model is delineated by Equation (2), while Equation (3) represents the pseudo-second-order kinetic model. Here,  $Q_t$  and  $Q_e$  represent the adsorption capacity at time  $t$  and at equilibrium (mg/g), respectively. The parameter  $b$  denotes the rate constant for the first-order equation (1/min), and  $k$  signifies the rate constant for the second-order equation (g/mg·min).

$$Q_t = Q_e \left[ 1 - e^{(-kt)} \right] \quad (2)$$

$$\frac{t}{Q_t} = \frac{1}{k_2 Q_e^2} + \frac{t}{Q_e} \quad (3)$$

#### 2.4. Characterization Testing

The elemental composition and concentrations of coal gangue and aluminum ash were determined employing X-ray fluorescence spectroscopy (PANalytical Zetium, Malvern Panalytical, Shanghai, China). The crystalline structure of the samples was elucidated via X-ray diffraction analysis (Shimadzu XRD-6000, Shimadzu Corporation, Kyoto, Japan). Microscopic examination of the sample morphology was conducted utilizing a scanning electron microscope (Hitachi Regulus8100, Hitachi, Tokyo, Japan). Quantitative and qualitative analysis of the samples was performed using an energy-dispersive X-ray spectrometer (IXRF Model 550i, Ixrf Systems, Austin, TX, USA) in conjunction with the scanning electron microscope. Further microscopic characterization of sample morphology was carried out employing a transmission electron microscope (FEI Talos F200X G2, Thermo Fisher Scientific, Waltham, MA, USA). Surface elemental composition and chemical states of the samples were investigated using X-ray photoelectron spectroscopy (ESCALAB Xi+, Thermo Fisher Scientific, Waltham, MA, USA). The functional groups of the samples were analyzed using a Nicolet 380 Fourier-transform infrared spectrometer. The absorbance of the solution was measured using a ultraviolet-visible (UV-Vis) spectrophotometer (PE Lambda 950, PerkinElmer, Waltham, MA, USA).

### 3. Results and Discussion

#### 3.1. Analysis of Coal Gangue

The predominant components of coal gangue were ascertained via X-ray fluorescence spectroscopy (XRF) analysis, revealing a significant presence of 61.72% SiO<sub>2</sub>, 25.74% Al<sub>2</sub>O<sub>3</sub>, and assorted compounds (as delineated in Table 1). With SiO<sub>2</sub> and Al<sub>2</sub>O<sub>3</sub> collectively comprising over 80% of the coal gangue composition, they can effectively serve as alternatives to pure silicon and aluminum sources in the synthesis of molecular sieves.

**Table 1.** Chemical composition of coal gangue powder (wt%).

SiO <sub>2</sub>	Al <sub>2</sub> O <sub>3</sub>	Fe <sub>2</sub> O <sub>3</sub>	CaO	MgO	K <sub>2</sub> O	Na <sub>2</sub> O	TiO <sub>2</sub>	MnO <sub>2</sub>	P <sub>2</sub> O <sub>5</sub>
57.00	28.29	5.34	2.61	0.85	1.46	0.77	1.11	0.07	0.06

Utilizing X-ray diffraction analysis (XRD), a qualitative examination of the crystalline phase structure of coal gangue material was conducted, as illustrated in Figure 4. It is discernible from the results that the pulverized coal gangue powder predominantly manifests silica–alumina components in the forms of quartz and kaolinite, indicative of stable structures with relatively subdued reactivity. Consequently, prior to the synthesis of molecular sieves, further activation treatment is imperative.

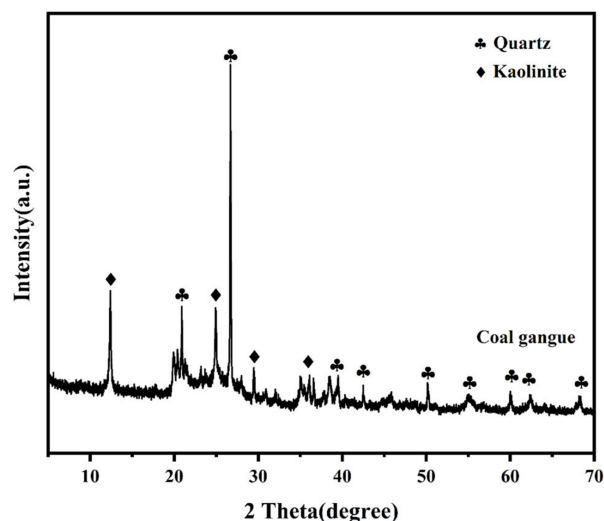


Figure 4. XRD analysis of coal gangue.

The coal gangue powder, subjected to a 2 h calcination at 900 °C, was meticulously blended with sodium hydroxide (NaOH) in a 1:2 mass ratio, followed by ball milling for homogenization. The resulting mixture was then subjected to a 2 h calcination at 500 °C in a crucible and subsequently cooled in the furnace before retrieval. The XRD pattern of the coal gangue powder post-alkali fusion is delineated in Figure 5. Post-alkali fusion, the kaolinite phase of the coal gangue, was eliminated, and the intensity of the quartz peak substantially diminished, concomitantly with the emergence of muscovite, calcite, sodalite, and calcium ferrite crystalline phases. In contrast to the inert quartz phase, muscovite and sodalite exhibit heightened reactivity, facilitating the dissolution and reorganization of silicon–aluminum constituents, thus facilitating the synthesis of molecular sieves via hydrothermal methodologies.

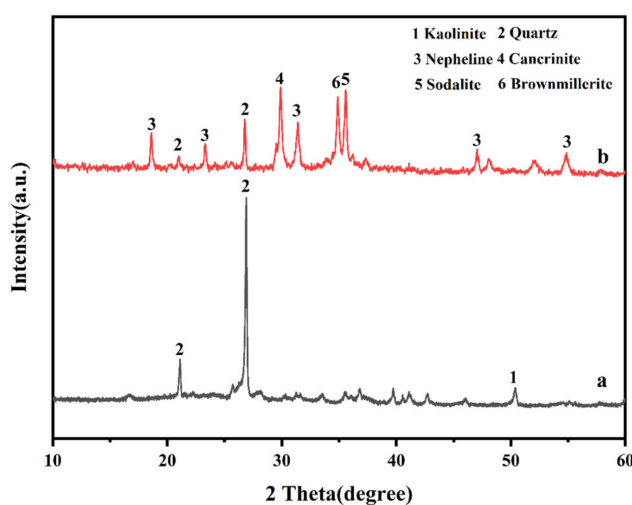
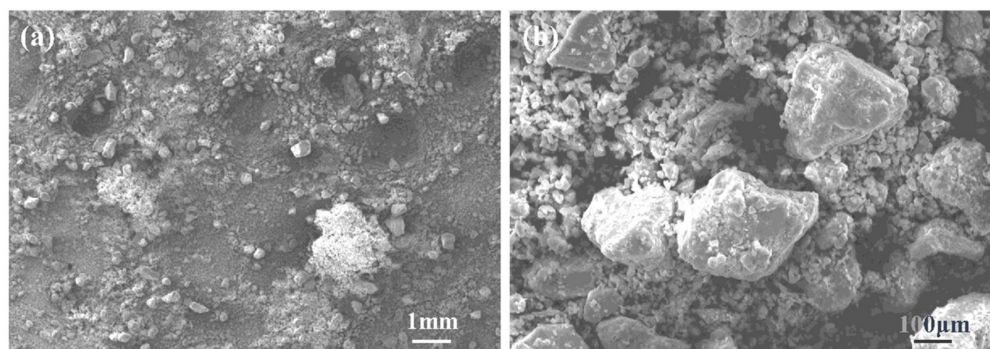


Figure 5. XRD analysis of coal gangue before and after alkali melting: (a) coal gangue before alkali melting treatment; (b) coal gangue after alkali melting treatment.

Microscopic examination of the morphology of coal gangue powder was performed using a scanning electron microscope (SEM), revealing characteristics depicted in Figure 6, primarily featuring irregular, fine particulate matter.



**Figure 6.** SEM image of coal gangue: (a) the magnification factor is 100; (b) the magnification factor is 1 k.

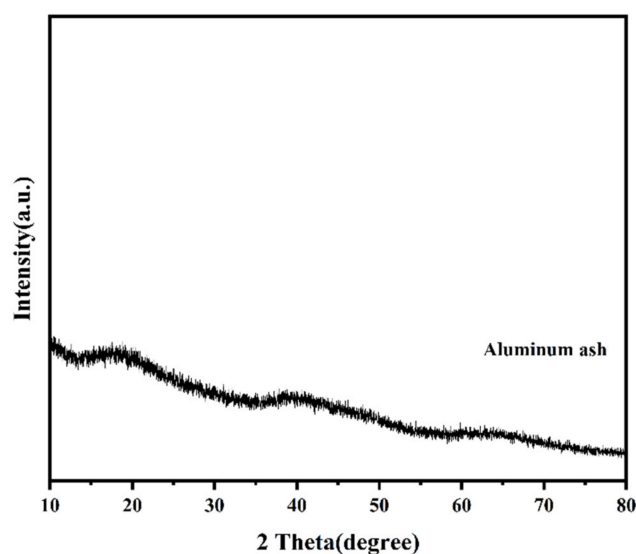
### 3.2. Analysis of Aluminum Ash

The XRF analysis outcomes, as delineated in Table 2, reveal that  $\text{Al}_2\text{O}_3$  constitutes approximately 80% of the composition of aluminum ash. This substantial fraction renders it suitable for substituting pure aluminum sources, enabling the adjustment of the silicon–aluminum ratio and facilitating the synthesis of molecular sieves through co-blending with coal gangue.

**Table 2.** Chemical composition of aluminum ash (wt%).

$\text{SiO}_2$	$\text{Al}_2\text{O}_3$	$\text{Fe}_2\text{O}_3$	$\text{CaO}$	$\text{MgO}$	$\text{SO}_3$	$\text{CuO}$	$\text{Na}_2\text{O}$	$\text{NiO}$	$\text{ZnO}$
1.56	79.08	0.61	2.33	1.20	11.43	0.28	1.59	0.16	0.01

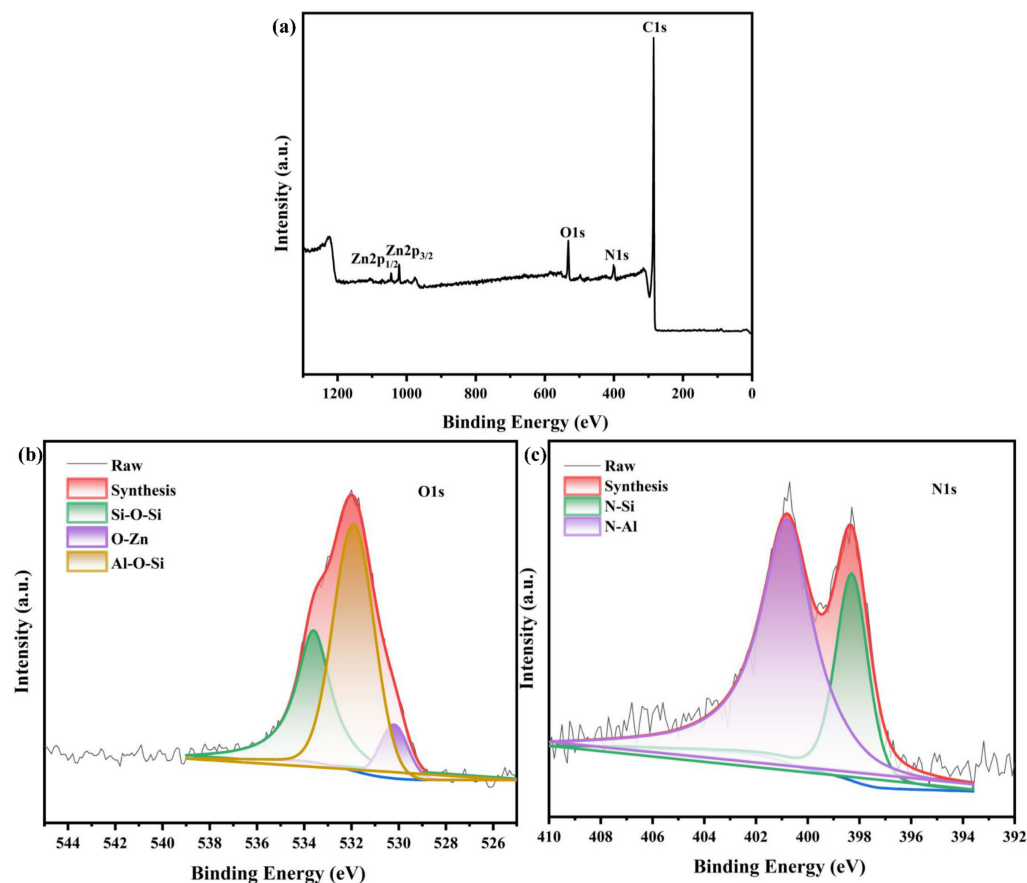
The XRD pattern of aluminum ash, as depicted in Figure 7, exhibits an amorphous phase. To discern the specific form in which aluminum elements are present, aluminum ash underwent analysis via energy-dispersive X-ray spectroscopy (EDS) and X-ray photoelectron spectroscopy (XPS), yielding the results presented in Table 3 and Figure 8, respectively. The analysis indicates that aluminum elements predominantly exist in the forms of oxides and nitrides.



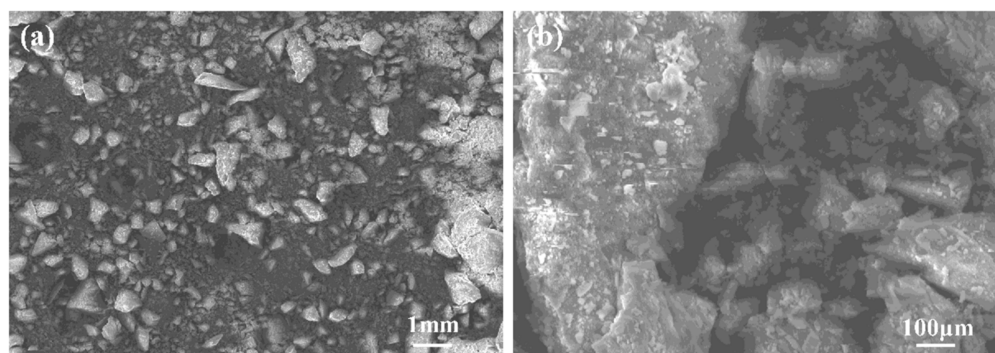
**Figure 7.** XRD analysis of aluminum ash.

**Table 3.** EDS results of aluminum ash (wt%).

Al	O	N	S	P	Si	Mg	Zn
41.686	41.233	10.686	2.062	1.960	1.571	0.802	0.007

**Figure 8.** XPS analysis of aluminum ash: (a) full spectrum; (b) O1s spectrogram; (c) N1s spectrogram.

SEM analysis of aluminum ash was conducted, yielding the results depicted in Figure 9, which showcased a predominance of irregular, fine particulate morphology, consistent with observations from the coal gangue powder analysis.

**Figure 9.** SEM image of aluminum ash: (a) the magnification factor is 100; (b) the magnification factor is 1 k.

### 3.3. Coal Gangue and Aluminum Ash Hydrothermal Synthesis of LTA-Type Molecular Sieve

Aluminum ash, in conjunction with alkali-treated coal gangue in different ratios, was utilized as a raw material for the hydrothermal synthesis of molecular sieves, following the

specific protocol outlined in Table 4. The synthesis of zeolite involved an aging period at 30 °C for 4 h followed by a crystallization step at 110 °C for 5 h.

**Table 4.** Scheme for hydrothermal synthesis of molecular sieves from coal gangue and aluminum ash.

Number	m (Coal Gangue:NaOH:Aluminum Ash)		
	Coal Gangue	NaOH	Aluminum Ash
w	1:2 (alkali fusion)		—
a	1:2 (alkali fusion)		0.25
b	1:2 (alkali fusion)		0.5
c	1:2 (alkali fusion)		1

### 3.3.1. Analysis of Crystal Structure

From Figure 10, it is discernible that under the synthesis conditions of 30 °C for 4 h of aging and 110 °C for 5 h of crystallization, utilizing solely coal gangue as the precursor yields a NaX-type molecular sieve. However, when the mass ratio of coal gangue to aluminum ash is 1:0.25, a conspicuous reduction in the characteristic peaks of the NaX molecular sieve is observed, coupled with an augmentation in the intensity of the LTA-type molecular sieve's characteristic peaks. As the quantity of aluminum ash added increases gradually, a greater number of characteristic peaks corresponding to LTA-type molecular sieves emerge, with their intensity showing a progressive augmentation. The XRD findings unequivocally demonstrate that with the escalating proportion of aluminum ash and the ensuing reduction in the silicon–aluminum ratio, a crystalline transition transpires from a NaX-type to an LTA-type molecular sieve.

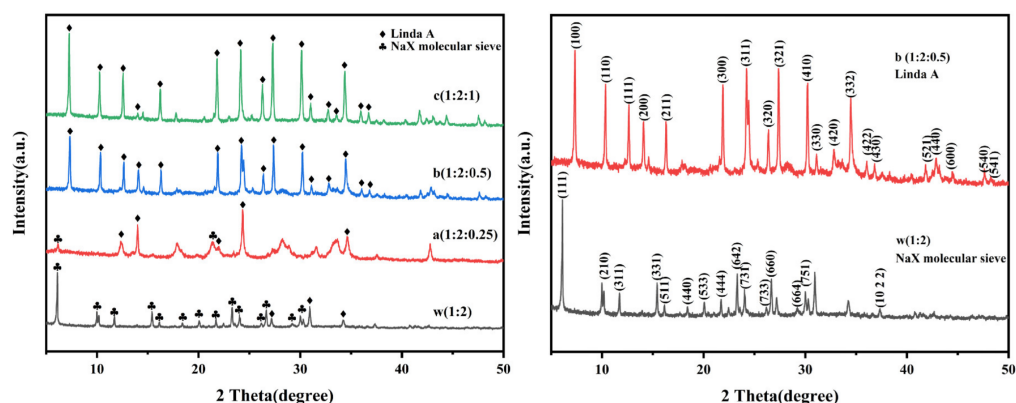


**Figure 10.** XRD patterns of products obtained by aging at 30 °C for 4 h and crystallizing at 110 °C for 5 h with different raw material ratios. (The standardized PDF card for the NaX-type molecular sieve can be referenced from Table S1; the standardized PDF card for the LTA-type molecular sieve can be referenced from Table S2.)

The transition from pure coal gangue to a composite of coal gangue and aluminum ash at a prescribed mass ratio induces a reduction in the silica-to-alumina ratio within the resultant molecular sieve framework. This denotes a heightened substitution of Si-O<sub>4</sub> tetrahedra by Al-O<sub>4</sub> tetrahedra within the molecular sieve matrix. The Al-O bond length typically ranges between 1.75 and 2.0 angstroms, while the bond angle spans approximately 90° to 109.5°. In contrast, the Si-O bond length typically falls within 1.60 to 1.65 angstroms, with a bond angle of around 109.5° for silicon tetrahedra. Consequently, the Al-O<sub>4</sub> tetrahedra exhibit elongated bond lengths and diminished bond angles. With an escalation in the abundance of Al-O<sub>4</sub> tetrahedra, the prevailing connectivity patterns undergo discernible alterations. As illustrated in Figure 11, the NaX-type molecular sieve embodies an FAU-type framework, with both FAU and LTA types rooted in the sodalite (SOD) cage architecture [29,30]. When SOD cages are arrayed in a simple cubic lattice and

interconnected via d4r rings, the resultant formation of an  $\alpha$ -cage at the unit cell's core engenders an overarching LTA-type framework. Conversely, a densely packed hexagonal arrangement of SOD cages, connected via d4r rings, yields an FAU-type framework [31]. Hence, upon the integration of aluminum ash to modulate the silica-to-alumina ratio of the product, the fundamental unit's bonding configurations within the molecular sieve undergo a transformative shift, thereby influencing the crystalline structure of the end product.

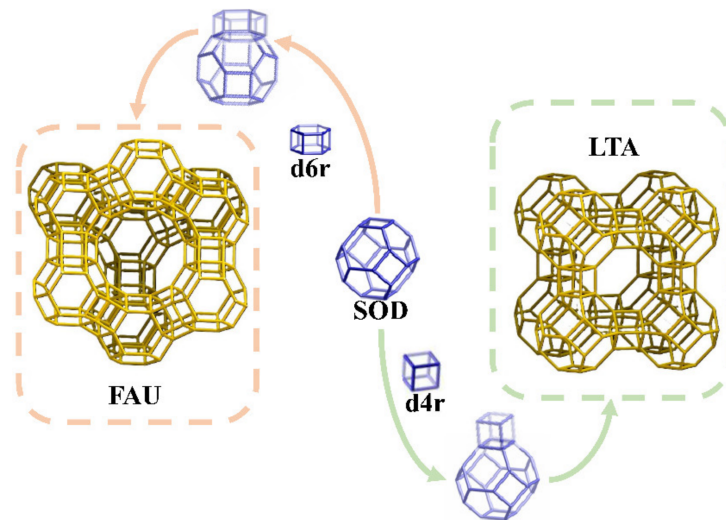


**Figure 11.** Structural transformation of FAU and LTA molecular sieve skeletons.

Figure 12 illustrates the XRD spectra of the products synthesized under a constant mass ratio of coal gangue to aluminum ash at 1:0.5, while varying the duration of crystallization. It is evident from the data that as the crystallization duration extends from 4 h to 5 h, the intensity of the characteristic peaks associated with the LTA-type molecular sieve increases, indicating a heightened degree of crystalline perfection. However, with further prolongation of the crystallization period, the intensity of these peaks diminishes, signaling a transition toward the sodalite structure. This phenomenon conforms to the Ostwald rule of successive transformations, where extended crystallization times favor the formation of the more thermodynamically stable sodalite phase from the initial LTA phase.

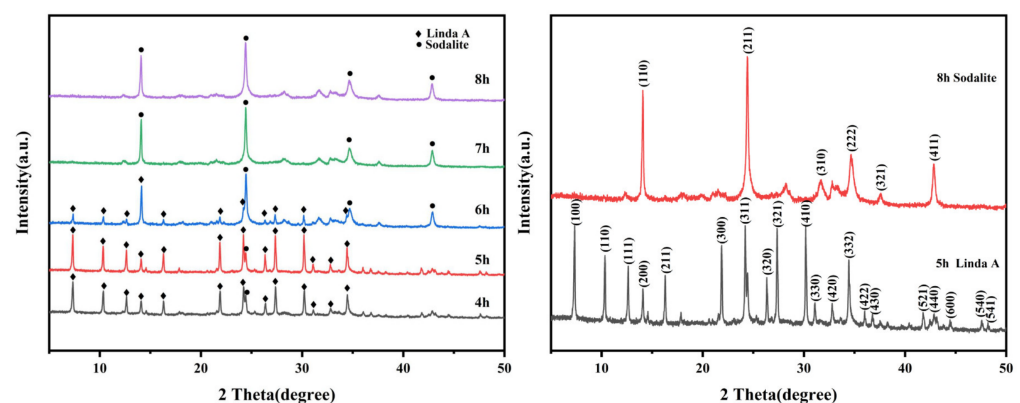


**Figure 12.** XRD patterns of products obtained by aging at 30 °C for 4 h and crystallizing at 110 °C for different durations (coal gangue to aluminum ash mass ratio of 1:0.5). (The standardized PDF card for the sodalite can be referenced from Table S3.)

### 3.3.2. Morphological Analysis

The microstructural analysis of the resultant products synthesized at varying coal gangue-to-aluminum ash mass ratios was conducted, focusing on their SEM morphology.

In Figure 13, distinct morphologies were observed corresponding to different ratios. Notably, the pure coal gangue synthesis yielded a cubic NaX-type molecular sieve, depicted in Figure 13w. At present, the raw material exhibits a silica-to-alumina ratio of 3.43. Conversely, when the coal gangue-to-aluminum ash mass ratio was 1:0.25, the synthesized product exhibited a tetrahedral LTA-type molecular sieve structure, as illustrated in Figure 13a. Furthermore, an evident trend was observed, wherein an increase in aluminum ash content led to a morphological transition from tetrahedral to lamellar-stacked spherical structures. As depicted in Figure 13c, the predominant morphology at this juncture manifests as stacked spherical layers, while maintaining a silica-to-alumina ratio of 1.45 in the raw material.

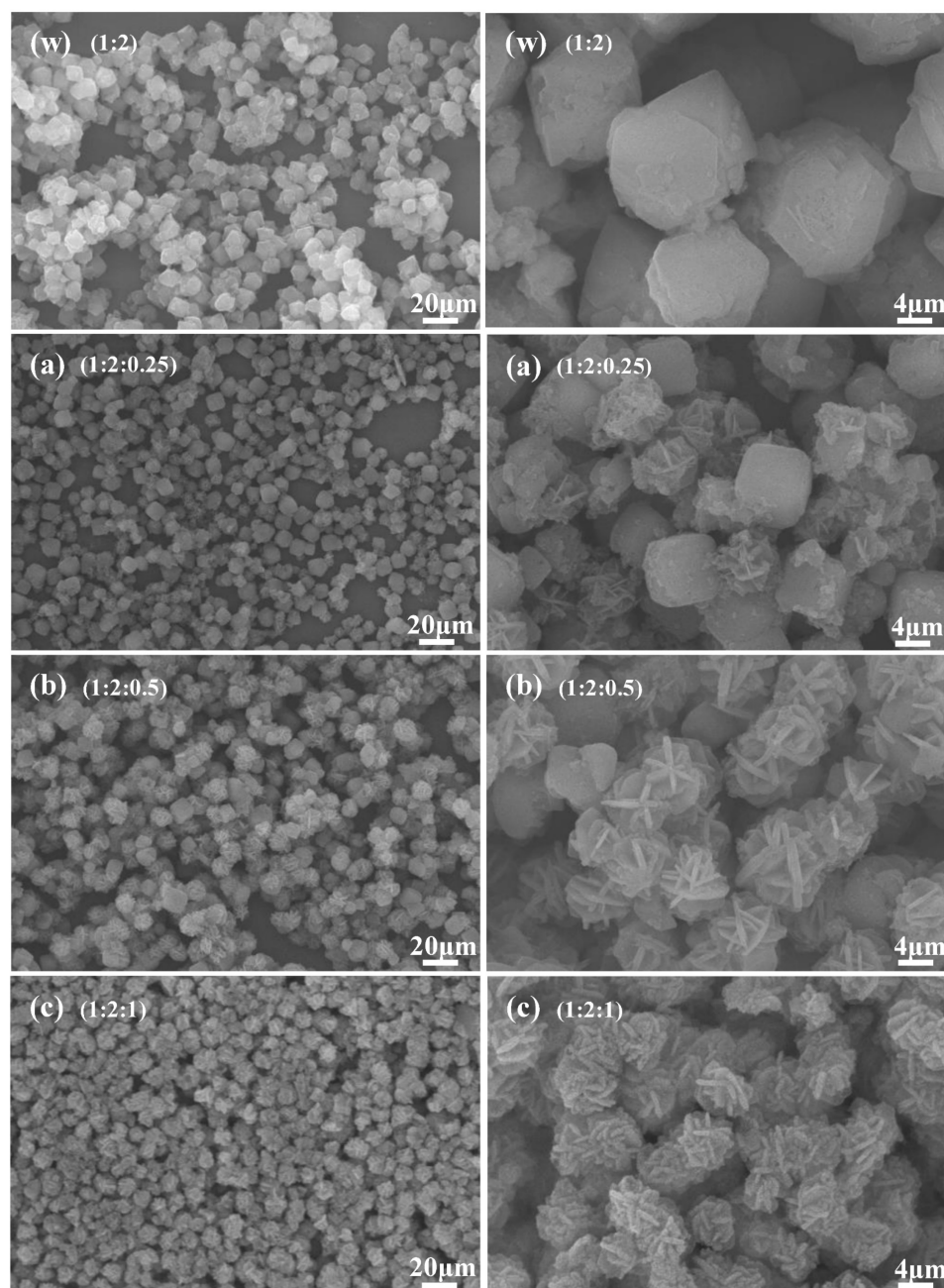


**Figure 13.** SEM image of products obtained by aging at 30 °C for 4 h and crystallizing at 110 °C for 5 h with different raw material ratios. (Refer to Table 4 for details on w, a, b, and c.)

EDS analysis was performed on the two distinct morphologies of products, as illustrated in Figure 14. The results revealed similar silicon-to-aluminum ratios between

the specimens; nevertheless, the tetrahedral-type molecular sieve exhibited a marginally higher silicon-to-aluminum ratio compared to the lamellar-stacked spherical structure. This observation concurs with the systematic addition of aluminum ash during synthesis. Furthermore, TEM imaging, as depicted in Figure 15, revealed that the lamellar-stacked spherical molecular sieves generally exhibited smaller dimensions than their tetrahedral counterparts and displayed a propensity for agglomeration and stacking.

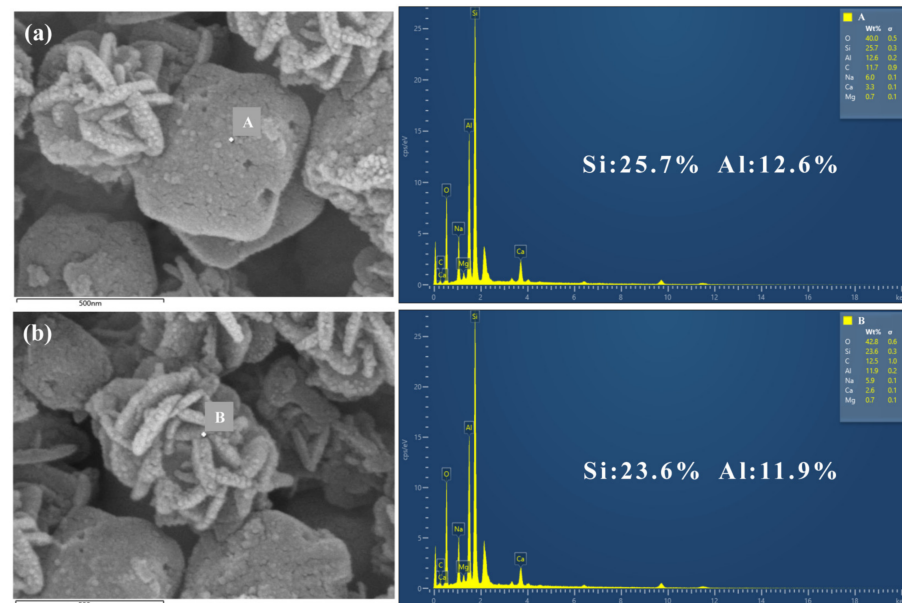


**Figure 14.** EDS results of products with different morphologies: (a) tetrahedra; (b) layer-by-layer stacked spherical shape.

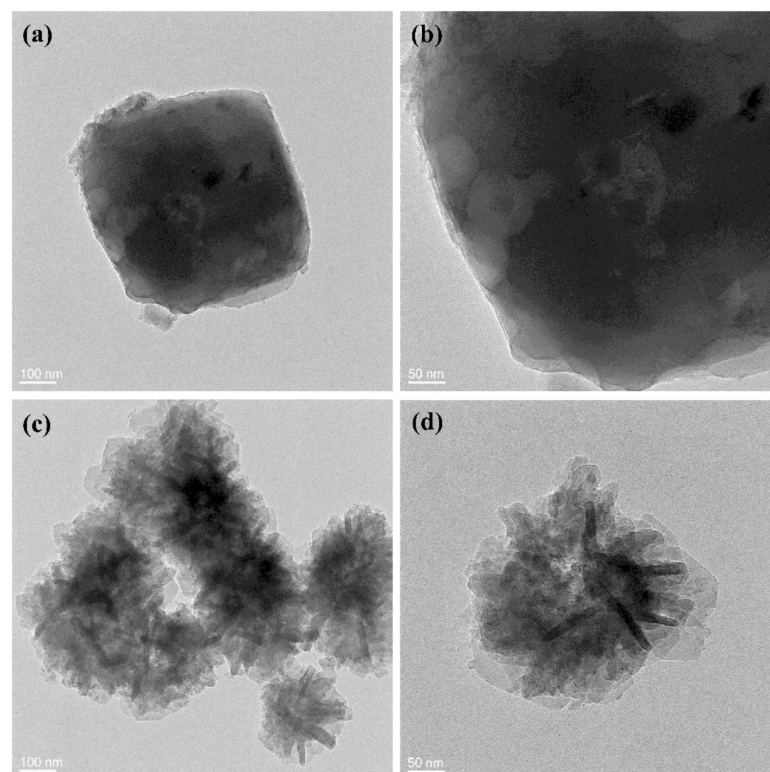


**Figure 15.** TEM images of products with different morphologies: (a,b) tetrahedra; (c,d) layer-by-layer stacked spherical shape.

The interplanar distances of the tetrahedral and lamellar-stacked spherical configurations of molecular sieves were computed, as depicted in Figure 16. Specifically, the tetrahedral-type molecular sieve exhibited an interplanar spacing of approximately 1.16 nm, while the lamellar-stacked spherical molecular sieve showed an interplanar spacing of approximately 0.86 nm. Comparing these computed interplanar spacings with the reference values from Table S2 of the LTA-type molecular sieve standard PDF cards, it becomes apparent that the tetrahedral morphology predominantly develops along the (100) crystallographic planes, whereas the lamellar-stacked spherical morphology predominantly emerges along the (110) crystallographic planes.

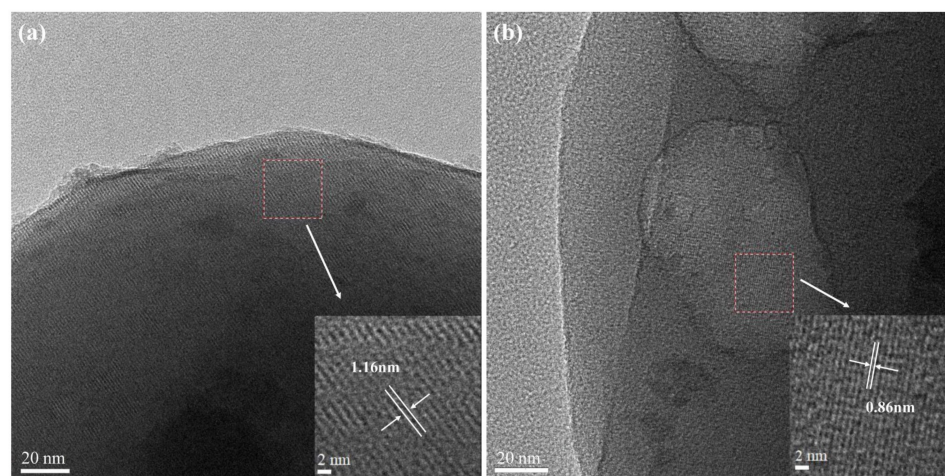


**Figure 16.** The interplanar spacing of products with different morphologies: (a) tetrahedra; (b) layer-by-layer stacked spherical shape.

### 3.4. Analysis of Adsorption Performance

#### 3.4.1. Comparative Analysis of Adsorption Performance between Prepared Product and Raw Materials

We experimented on  $\text{Cu}^{2+}$  adsorption using calcined coal gangue and aluminum ash, and prepared the molecular sieve separately (initial concentration: 150 mg/L, solid–liquid ratio: 2 g/L, adsorption temperature: 25 °C, adsorption duration: 8 h). As depicted in Figure 17, the adsorption outcomes suggest an enhancement in the adsorption efficiency of the synthesized LTA-type molecular sieve compared to the raw materials. As the proportion of aluminum ash increases, there is an observed trend of optimization in adsorption efficacy. When the mass ratio of coal gangue to aluminum ash is 1:0.5 and 1:1, respectively, the theoretical silica-to-alumina ratios of the raw materials are 1.45 and 0.93. However, in actual synthesis, experimental conditions and the Lowenstein rule impose constraints [32]. Both ratios of silica to alumina are close to each other. This is also evident from Figure 10, where the synthesized products for both ratios are A-type molecular sieves. Hence, the adsorption efficacy of both is similar. Subsequent adsorption experiments will be conducted using the molecular sieve (b) prepared from a coal gangue-to-aluminum ash mass ratio of 1:0.5.

#### 3.4.2. The Effect of Adsorption Time on the Adsorption Performance of $\text{Cu}^{2+}$

Under conditions where the initial concentration of  $\text{Cu}^{2+}$  in solution was set at 150 mg/L, with a solid-to-liquid ratio of 2 g/L and at an adsorption temperature of 25 °C, the adsorption of  $\text{Cu}^{2+}$  was investigated over a duration spanning from 90 min to 240 min. The adsorption outcomes are depicted in Figure 18. Notably, the adsorption process exhibited a dual-phase behavior characterized by an initial phase of rapid adsorption within the first 120 min, followed by a subsequent phase of slower adsorption kinetics. By the 240 min mark, an adsorption equilibrium was nearly attained. Remarkably, after 120 min of adsorption, the concentration of  $\text{Cu}^{2+}$  declined to 0.9825 mg/L, aligning with the stipulated national standard for  $\text{Cu}^{2+}$  content in potable water (<1 mg/L) [33], and achieving a  $\text{Cu}^{2+}$

removal rate exceeding 99%. These results underscore the remarkable  $\text{Cu}^{2+}$  adsorption efficacy of the synthesized LTA-type molecular sieve.

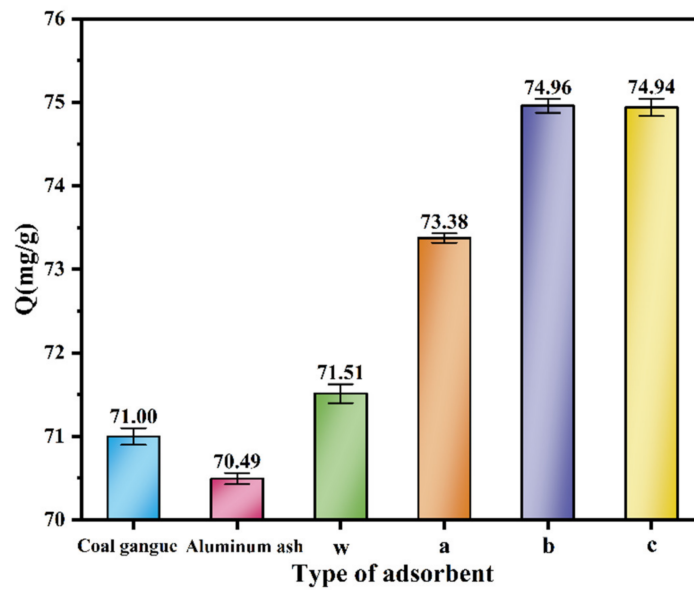


Figure 17. Results of adsorption of  $\text{Cu}^{2+}$  solution on different adsorbents.

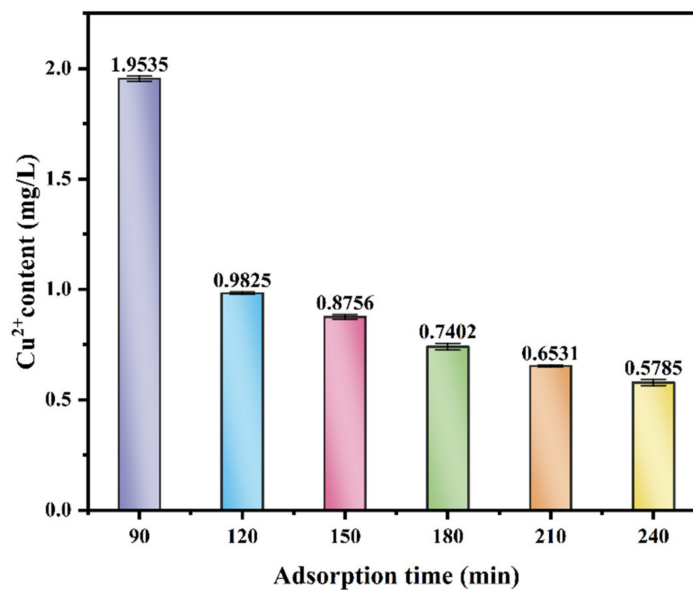
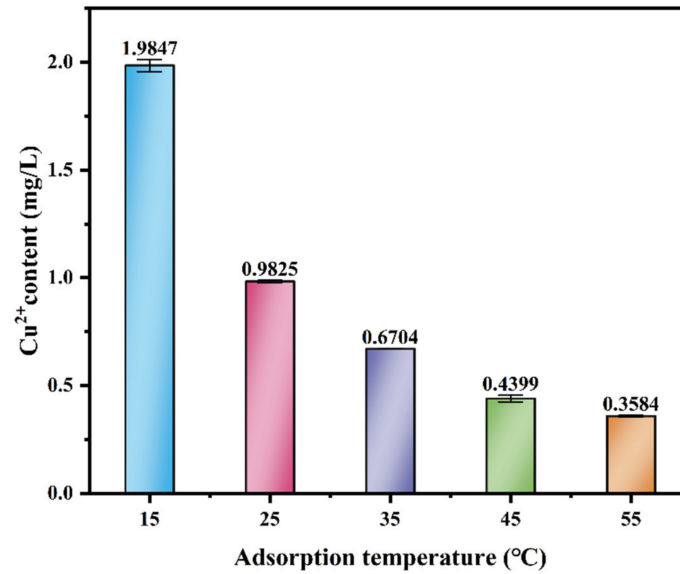


Figure 18. Results of adsorption of  $\text{Cu}^{2+}$  solution on LTA-type molecular sieve at different times.

### 3.4.3. The Effect of Adsorption Temperature on the Adsorption Performance of $\text{Cu}^{2+}$

Under the experimental conditions with an initial  $\text{Cu}^{2+}$  concentration of 150 mg/L, a solid-to-liquid ratio of 2 g/L, and an adsorption duration of 120 min, investigations were conducted across temperatures ranging from 15 °C to 55 °C. The results of the adsorption experiments are depicted in Figure 19. Notably, an ascending trend in  $\text{Cu}^{2+}$  removal efficiency was observed with increasing adsorption temperatures. This phenomenon can be elucidated by two primary factors. Firstly, the elevation in temperature induces a decline in aqueous solution viscosity, consequently diminishing the hydration level of  $\text{Cu}^{2+}$  ions and augmenting the affinity of cations towards adsorption sites. Moreover, the reduction in solution viscosity amplifies mass transfer diffusion coefficients, thereby accelerating the adsorption kinetics.



**Figure 19.** Results of adsorption of Cu<sup>2+</sup> solution on LTA-type molecular sieve at different temperatures.

#### 3.4.4. The Effect of Initial Concentration on the Adsorption Performance of Cu<sup>2+</sup>

Under the conditions of a solid–liquid ratio of 2 g/L, an adsorption temperature of 25 °C, and an adsorption duration of 120 min, Cu<sup>2+</sup> solutions with initial concentrations ranging from 50 to 250 mg/L were individually subjected to adsorption. The resultant adsorption trends are depicted in Figure 20. It is evident from Figure 20 that, with increasing initial concentrations, the removal efficiency of the specimens progressively diminishes. This phenomenon may be attributed to the concentration-dependent nature of the adsorption process regarding Cu<sup>2+</sup>. At lower concentrations, the molecular sieve fails to achieve saturation adsorption, whereas, with escalating initial concentrations of Cu<sup>2+</sup>, the adsorption capacity of the specimens gradually approaches saturation. Consequently, the surplus of unadsorbed Cu<sup>2+</sup> escalates, precipitating a reduction in removal efficiency.

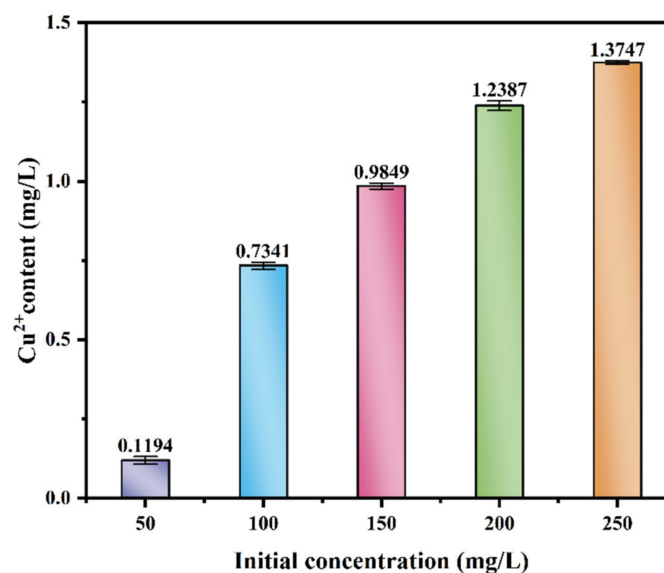
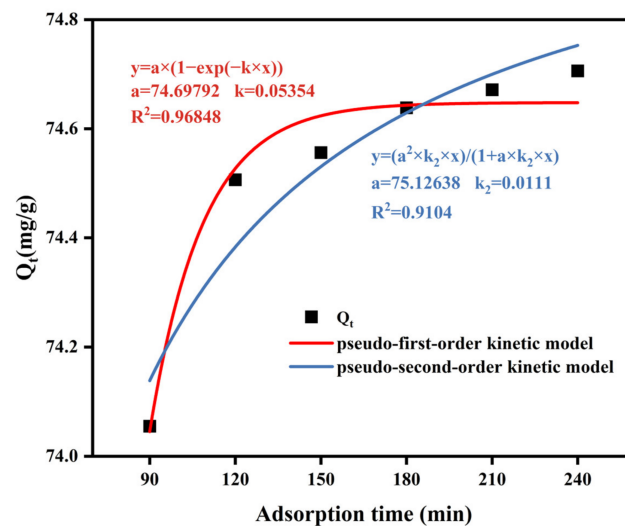


**Figure 20.** Results of LTA-type molecular sieve adsorption of Cu<sup>2+</sup> solutions with different initial concentrations.

#### 3.4.5. Adsorption Kinetics Simulation

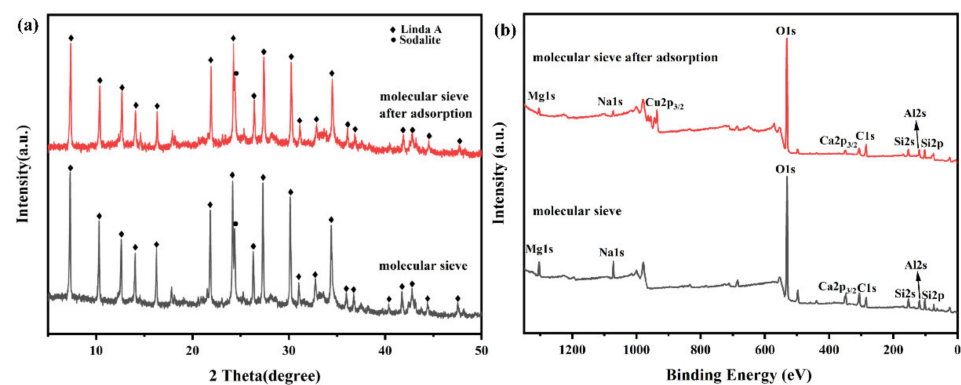
To delve into the adsorption mechanism, assessments of the Cu<sup>2+</sup> concentration in the solution post varying adsorption durations were conducted, and the corresponding

adsorption quantities were computed for adsorption kinetics modeling. The adsorption capacity  $Q_t$  was derived using Equation (1). Subsequently, nonlinear fitting of the adsorption data was performed employing both the pseudo-first-order and pseudo-second-order kinetic models, as depicted in Figure 21. Notably, the pseudo-second-order kinetic model demonstrated superior fitting efficacy, indicating a concomitance of physical and chemical adsorption processes, with chemical adsorption predominating. During  $\text{Cu}^{2+}$  adsorption by the molecular sieve, a fraction of  $\text{Cu}^{2+}$  ions undergoes direct ingress into the molecular sieve pores via physical adsorption, while the residual portion undergoes chemical adsorption.



**Figure 21.** Dynamics results and fitting curve of adsorption of  $\text{Cu}^{2+}$  on LTA-type molecular sieve.

To explore the adsorption mechanism during chemical adsorption, characterization tests were conducted on the molecular sieve before and after adsorption. From Figure 22a, it is evident that following adsorption, the molecular sieve exhibits a subtle displacement in its characteristic peak, accompanied by a reduction in intensity, which is due to the lattice defect of the molecular sieve after adsorption. In Table 5, the energy dispersive spectrometer (EDS) results revealed a decrease in Na, Mg, and Ca content and an increase in Cu content after adsorption, with the increment in Cu content being roughly equivalent to the reduction in Na, Mg, and Ca content. Similarly, XPS analysis of the molecular sieve before and after adsorption, as shown in Figure 22b, demonstrated that the Mg1s, Na1s, and Ca2p<sub>3/2</sub> characteristic peaks nearly disappeared, while the Cu2p characteristic peak appeared after adsorption. This indicates that during adsorption,  $\text{Cu}^{2+}$  ions undergo ion exchange with  $\text{Mg}^{2+}$ ,  $\text{Na}^+$ , and  $\text{Ca}^{2+}$  ions, originally counterbalancing the negative charges within the framework of the molecular sieve, and thereby inducing lattice defects.

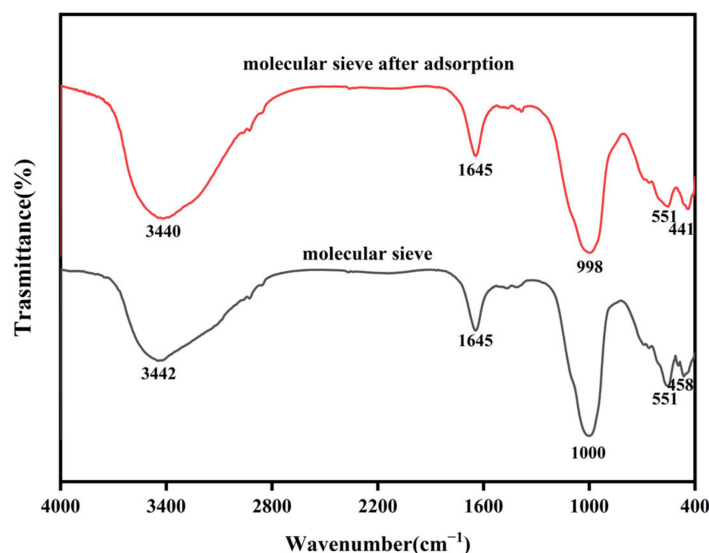


**Figure 22.** Molecular sieves before and after 120 min of adsorption of 150 mg/L  $\text{Cu}^{2+}$  solution: (a) XRD spectrum; (b) XPS spectrum.

**Table 5.** EDS results before and after adsorption (wt%) ((a) molecular sieve; (b) molecular sieve after 120 min of adsorption of 150 mg/L  $\text{Cu}^{2+}$  solution).

Sample \ Element	Na	Mg	Ca	Si	Al	Cu
a	13.953	8.953	3.953	22.324	14.927	—
b	1.556	3.776	2.631	23.898	11.313	17.292

Figure 23 illustrates the infrared spectra of LTA-type molecular sieves before and after adsorption. The absorption band around  $1000\text{ cm}^{-1}$  is attributed to the asymmetric stretching vibration of T-O-T bonds (T = Si or Al) [34], while the peak at approximately  $450\text{ cm}^{-1}$  corresponds to the symmetric stretching vibration of T-O bonds (T = Si or Al) [35]. Furthermore, the appearance of a peak at  $551\text{ cm}^{-1}$  indicates the characteristic vibration of double-four-ring (D4R) structures [36], indicating the presence of such structures within the LTA-type molecular sieves. Additionally, the O-H vibration peaks around  $3440\text{ cm}^{-1}$  and  $1645\text{ cm}^{-1}$  after adsorption are significantly enhanced and have a certain shift, which is due to the hydroxyl complexation of  $\text{Cu}^{2+}$  during adsorption [37].

**Figure 23.** FT-IR spectrum of molecular sieves before and after 120 min of adsorption of 150 mg/L  $\text{Cu}^{2+}$  solution.

Hence, when the molecular sieve is exposed to the  $\text{Cu}^{2+}$ -containing adsorption solution, a portion of the  $\text{Cu}^{2+}$  permeates the molecular sieve pores, undergoing physical adsorption, while the remaining fraction undergoes chemical adsorption. During chemical adsorption, a fraction of the  $\text{Cu}^{2+}$  ions undergo ion exchange reactions with the  $\text{Mg}^{2+}$ ,  $\text{Na}^+$ , and  $\text{Ca}^{2+}$  ions that originally balance the negative charges within the molecular sieve framework, while another fraction participates in hydroxyl complexation reactions, forming copper hydroxyl complexes.

#### 4. Conclusions

Utilizing coal gangue as the primary precursor and aluminum ash as an adjunct aluminum source, molecular sieves were synthesized under controlled conditions involving a 4 h aging period at  $30\text{ }^\circ\text{C}$  followed by a 5 h crystallization process at  $110\text{ }^\circ\text{C}$ . When sole coal gangue constituted the raw material, the resultant product exhibited a NaX-type molecular sieve configuration. Conversely, upon employing a blend of coal gangue and alumina ash for synthesis, the ensuing product showcased an LTA-type molecular sieve

architecture, with its prevalence escalating in tandem with the augmentation of aluminum ash proportion.

SEM and TEM analyses of the synthesized molecular sieves reveal the production of tetrahedral and lamellar-stacked spherical LTA-type molecular sieves derived from coal gangue and alumina ash. Specifically, when alumina ash constitutes a minor proportion, crystals exhibit growth along the (100) crystallographic planes, yielding molecular sieves with tetrahedral morphology. Conversely, with a gradual increase in the proportion of aluminum ash, crystal growth shifts towards other crystallographic planes, resulting in the formation of products exhibiting lamellar-stacked spherical morphology.

After adsorption of a 150 mg/L  $\text{Cu}^{2+}$  solution by LTA-type molecular sieves synthesized via hydrothermal treatment of coal gangue and aluminum ash at a mass ratio of 1:0.5 for 2 h, the resulting water meets the Chinese national drinking water standards. During the adsorption process, a portion of  $\text{Cu}^{2+}$  ions directly infiltrate into the pores of the molecular sieve, resulting in physical adsorption, while the remaining portion undergoes ion exchange reactions with the  $\text{Mg}^{2+}$ ,  $\text{Na}^+$ , and  $\text{Ca}^{2+}$  ions within the framework of the molecular sieve, which originally balance the negative charges, or participates in hydroxyl complexation reactions to form copper hydroxyl complexes.

**Supplementary Materials:** The following supporting information can be downloaded at: <https://www.mdpi.com/article/10.3390/cryst14040379/s1>, Table S1: NaX Molecular Sieve Standard PDF Card (PDF # 38-0237); Table S2: LTA Molecular Sieve Standard PDF Card (PDF # 11-0589); Table S3: Sodalite Standard PDF Card (PDF # 37-0196).

**Author Contributions:** All authors have contributed to the study's conception and design. Conceptualization, W.X. and Q.W.; methodology, J.C.; software, J.M.; validation, J.M.; investigation, W.X.; data curation, W.X.; writing—original draft, W.X.; writing—review and editing, Q.W., J.C. and Q.Y.; supervision, Q.W.; project administration, Q.W. All authors have read and agreed to the published version of the manuscript.

**Funding:** This research was funded by the National Natural Science Foundation of China (NSFC) [52227901]; the University Synergy Innovation Program of Anhui Province [GXXT-2022-083], [GXXT-2023-019]; and the Anhui Provincial Natural Science Foundation [2208085ME103].

**Data Availability Statement:** Data is contained within the article or Supplementary Materials.

**Conflicts of Interest:** The authors declare that there is no conflict of interest regarding the publication of this article.

## References

1. National Development and Reform Commission of China. Guiding Opinions on the Comprehensive Utilization of Bulk Solid Waste during the 14th Five Year Plan Period. 2021. Available online: [https://www.ndrc.gov.cn/xxgk/zcfb/tz/202103/t20210324\\_1270286.html](https://www.ndrc.gov.cn/xxgk/zcfb/tz/202103/t20210324_1270286.html) (accessed on 12 March 2024).
2. Li, J.; Wang, J. Comprehensive utilization and environmental risks of coal gangue: A review. *J. Clean. Prod.* **2019**, *239*, 117946. [[CrossRef](#)]
3. Ministry of Ecology and Environment of the People's Republic of China. 2022 China Ecological Environment Status Bulletin. 2023. Available online: <https://www.mee.gov.cn/hjzl/sthjzk/zghjzkqb/202305/P020230529570623593284.pdf> (accessed on 12 March 2024).
4. Ouyang, S.; Huang, Y.; Gao, H.; Guo, Y.; Wu, L.; Li, J. Study on the distribution characteristics and ecological risk of heavy metal elements in coal gangue taken from 25 mining areas of China. *Environ. Sci. Pollut. Res.* **2022**, *29*, 48285–48300. [[CrossRef](#)] [[PubMed](#)]
5. Song, S.; Peng, R.; Wang, Y.; Cheng, X.; Niu, R.; Ruan, H. Spatial distribution characteristics and risk assessment of soil heavy metal pollution around typical coal gangue hill located in Fengfeng Mining area. *Environ. Geochem. Health* **2023**, *45*, 7215–7236. [[CrossRef](#)] [[PubMed](#)]
6. Yang, D.; Li, J.; Huang, Y.; Song, T.; Gao, H.; Qiao, M. Research on Migration Law of Mn in Mudstone Floor in the Goaf under Coupling Conditions of Seepage and Stress. *Pol. J. Environ. Stud.* **2020**, *29*, 939–950. [[CrossRef](#)]
7. Zhang, Y.; Liu, Y.; Liu, J.; Zhan, R.; He, W.; Tong, L.; Wan, P.; Bai, L. Control mechanism of the migration of heavy metal ions from gangue backfill bodies in mined-out areas. *Front. Earth Sci.* **2023**, *10*, 1090799. [[CrossRef](#)]

8. Meng, F.; Yu, J.; Tahmasebi, A.; Han, Y. Pyrolysis and Combustion Behavior of Coal Gangue in O<sub>2</sub>/CO<sub>2</sub> and O<sub>2</sub>/N<sub>2</sub> Mixtures Using Thermogravimetric Analysis and a Drop Tube Furnace. *Energy Fuels* **2013**, *27*, 2923–2932. [CrossRef]
9. Li, J.; Chen, L.; Luo, J.; Zhu, W.; Fan, X.; Zhu, Y.; Zhang, Z. Mechanical properties and microscopic characteristics of steel fiber coal gangue concrete. *Front. Mater.* **2023**, *10*, 1211129. [CrossRef]
10. Li, M.; Peng, Y.; Ding, L.; Zhang, J.; Ma, D.; Huang, P. Analysis of Surface Deformation Induced by Backfill Mining Considering the Compression Behavior of Gangue Backfill Materials. *Appl. Sci.* **2023**, *13*, 160. [CrossRef]
11. Yang, J.; Tian, L.; Meng, L.; Wang, F.; Die, Q.; Yu, H.; Yang, Y.; Huang, Q. Thermal utilization techniques and strategies for secondary aluminum dross: A review. *J. Environ. Manag.* **2024**, *351*, 119939. [CrossRef]
12. Cinarli, U.; Turan, A. Investigation of Alumina-Based Ceramic Production from Aluminum Black Dross. *Min. Metall. Explor.* **2021**, *38*, 257–267. [CrossRef]
13. David, E.; Kopac, J. Aluminum recovery as a product with high added value using aluminum hazardous waste. *J. Hazard. Mater.* **2013**, *261*, 316–324. [CrossRef]
14. Mahinroosta, M.; Allahverdi, A. Hazardous aluminum dross characterization and recycling strategies: A critical review. *J. Environ. Manag.* **2018**, *223*, 452–468. [CrossRef]
15. National Bureau of Statistics of China. Statistical Bulletin on National Economic and Social Development of the People's Republic of China in 2023. 2024. Available online: [https://www.stats.gov.cn/sj/zxfb/202402/t20240228\\_1947915.html](https://www.stats.gov.cn/sj/zxfb/202402/t20240228_1947915.html) (accessed on 12 March 2024).
16. Liu, Y.; Yang, J.; Shen, H.; Zhang, J.; Li, W.; Zhang, X.; Liu, J.; Liu, B.; Zhang, S. Synthesis of porous glass ceramics with hierarchical and interconnected pores from secondary aluminum dross and waste glass. *Ceram. Int.* **2022**, *48*, 34364–34373. [CrossRef]
17. Yuan, H.; Luo, T.; Zhang, D.; Wang, Q. Harmless treatment and recycling of secondary aluminum dross: A review. *J. Sustain. Cem.-Based Mater.* **2023**, *12*, 1460–1473. [CrossRef]
18. Meshram, A.; Singh, K.K. Recovery of valuable products from hazardous aluminum dross: A review. *Resour. Conserv. Recycl.* **2018**, *130*, 95–108. [CrossRef]
19. Du, J.; Ma, A.; Wang, X.; Zheng, X. Review of the Preparation and Application of Porous Materials for Typical Coal-Based Solid Waste. *Materials* **2023**, *16*, 5434. [CrossRef] [PubMed]
20. Wang, B.; Li, L.; Li, J.; Jin, K.; Zhang, S.; Zhang, J.; Yan, W. Recent Progresses on the Synthesis of Zeolites from the Industrial Solid Wastes. *Chem. J. Chin. Univ.-Chin.* **2021**, *42*, 40–59. [CrossRef]
21. Coronas, J. Present and future synthesis challenges for zeolites. *Chem. Eng. J.* **2010**, *156*, 236–242. [CrossRef]
22. Zhang, X.; Li, C.; Zheng, S.; Di, Y.; Sun, Z. A review of the synthesis and application of zeolites from coal-based solid wastes. *Int. J. Miner. Metall. Mater.* **2022**, *29*, 1–21. [CrossRef]
23. Bieseki, L.; Penha, F.G.; Castella Pergher, S.B. Zeolite A Synthesis Employing a Brazilian Coal Ash as the Silicon and Aluminum Source and its Applications in Adsorption and Pigment Formulation. *Mater. Res.-Ibero-Am. J. Mater.* **2013**, *16*, 38–43. [CrossRef]
24. Rigo, R.T.; Pergher, S.B.C.; Petkowicz, D.I.; dos Santos, J.H.Z. A new procedure for a zeolite synthesis from natural clays. *Quim. Nova* **2009**, *32*, 21–25. [CrossRef]
25. Hu, C.; Yan, W.; Xu, R. Phase Transition Behavior of Zeolite Y under Hydrothermal Conditions. *Acta Chim. Sin.* **2017**, *75*, 679–685. [CrossRef]
26. Li, L.; Xu, S.; Liu, Z.; Wang, D. Insight into the Growth Mechanism of Low-Temperature Synthesis of High-Purity Lithium Slag-Based Zeolite A. *Materials* **2024**, *17*, 568. [CrossRef] [PubMed]
27. Ma, Z.; Deng, H.; Li, L.; Zhang, Q.; Chen, G.; Sun, C.; He, H.; Yu, J. Fluoride-free and seed-free microwave-assisted hydrothermal synthesis of nanosized high-silica Beta zeolites for effective VOCs adsorption. *Chem. Sci.* **2023**, *14*, 2131–2138. [CrossRef] [PubMed]
28. Ke, G.; Shen, H.; Yang, P. Synthesis of X-Zeolite from Waste Basalt Powder and its Influencing Factors and Synthesis Mechanism. *Materials* **2019**, *12*, 3895. [CrossRef] [PubMed]
29. Xing, E.; Shi, Y.; Xie, W.; Zhang, F.; Mu, X.; Shu, X. Size-controlled synthesis of MCM-49 zeolite from NaX for liquid-phase alkylation of benzene with ethylene. *Microporous Mesoporous Mater.* **2016**, *236*, 54–62. [CrossRef]
30. Xing, E.; Shi, Y.; Zheng, A.; Zhang, J.; Gao, X.; Liu, D.; Xin, M.; Xie, W.; Zhang, F.; Mu, X.; et al. Transformation from NaA to MCM-49 Zeolite and Its Catalytic Alkylation Performance. *Ind. Eng. Chem. Res.* **2015**, *54*, 3123–3135. [CrossRef]
31. Structure Commission of the International Zeolite Association (IZA-SC). Database of Zeolite Structures. Available online: <https://www.iza-structure.org/databases/> (accessed on 14 March 2024).
32. Maria Gomez, J.; Montes, I.; Diez, E.; Rodriguez, A. Mesoporous low silica X (MLSX) zeolite: Mesoporosity in loewenstein limit? *Microporous Mesoporous Mater.* **2022**, *330*, 111618. [CrossRef]
33. GB 5749-2022; Standards for Drinking Water Quality. Standardization Administration of the People's Republic of China, State Administration for Market Regulation of China: Beijing, China, 2022.
34. Iqbal, A.; Sattar, H.; Haider, R.; Munir, S. Synthesis and characterization of pure phase zeolite 4A from coal fly ash. *J. Clean. Prod.* **2019**, *219*, 258–267. [CrossRef]
35. Sivalingam, S.; Sen, S. Optimization of synthesis parameters and characterization of coal fly ash derived microporous zeolite X. *Appl. Surf. Sci.* **2018**, *455*, 903–910. [CrossRef]

- 
36. Wang, P.; Sun, Q. Synthesis and characterisation of zeolite LTA with sheet structure. *Micro Nano Lett.* **2020**, *15*, 433–436. [[CrossRef](#)]
  37. Chen, Y.; Dong, S.; Wei, S.; Zhang, S.; Zhang, J.; Gu, J. Green and efficient synthesis of mesoporous sodalite assisted by persulfate or peroxymonosulfate. *Microporous Mesoporous Mater.* **2022**, *346*, 112321. [[CrossRef](#)]

**Disclaimer/Publisher’s Note:** The statements, opinions and data contained in all publications are solely those of the individual author(s) and contributor(s) and not of MDPI and/or the editor(s). MDPI and/or the editor(s) disclaim responsibility for any injury to people or property resulting from any ideas, methods, instructions or products referred to in the content.